Available online at www.sciencedirect.com
ScienceDirect
Journal of Luminescence 128 (2008) 15–21
JOURNAL OF LUMINESCENCE
www.elsevier.com/locate/jlumin

Morphology-dependent upconversion luminescence of ZnO:Er^{3+} nanocrystals

Yajuan Sun[a,b,c], Yue Chen[a], Lijin Tian[b,c], Yi Yu[b], Xianggui Kong[b,**], Qinghui Zeng[b], Youlin Zhang[b], Hong Zhang[c,*]

[a]*College of Chemistry, Jilin University, Changchun 130023, PR China*
[b]*Key Laboratory of Excited State Process, Changchun Institute of Optics, Fine Mechanics and Physics, Chinese Academy of Sciences, Changchun 130033, PR China*
[c]*Van't Hoff Institute for Molecular Sciences, University of Amsterdam, Nieuwe Achtergracht 166, 1018 WV Amsterdam, The Netherlands*

Received 7 December 2006; received in revised form 13 April 2007; accepted 20 April 2007
Available online 27 April 2007

Abstract

Morphology impact on the upconverted luminescence of ZnO:Er^{3+} nanocrystals was studied with controllable morphology of nanorod, prickly sphere-like, column-like, branch rod, prism-like, and grain-like, prepared via the cetyltrimethylammonium bromide (CTAB)-assisted hydrothermal process. The upconversion emission of Er^{3+} with 980 nm excitation demonstrated morphology sensitivity which was related with the local environments of Er^{3+} ions in ZnO and doping efficiency. Under ultraviolet (UV) direct excitation, where exciton and defect emissions of ZnO appeared, morphology sensitivity was discussed in terms of surface-to-volume ratios.

Keywords: ZnO:Er^{3+}; Rare-earth ions; Upconversion; Luminescence; Morphology

1. Introduction

Recently, room-temperature ultraviolet (UV) lasing from ZnO nanorod arrays [1] and nanowire [2,3] has been obtained, highlighting the prospects of corresponding research interest in the fabrication of ZnO-based candidate materials. Besides, ZnO has been used as a host material for the visible and infrared emission of various rare-earth ions [4,5]. The Er^{3+} ion is probably the most widely studied among the rare-earth ions that show upconversion photoluminescence (UCP) because it provides the long-lived intermediate level $^4I_{11/2}$ easily accessible with a diode laser at 980 nm and has rather high upconversion efficiency. The evaluation of the photoluminescence (PL) properties [6], and the mechanisms of the energy transfer to Er^{3+} from the host semiconductors has been executed extensively [7–11]. Despite these efforts, the understanding on the morphology influence on the UCP is still lacking although it is rationally expected that the PL properties of ZnO:Er^{3+} should be closely related with its morphology.

In this paper, the morphology impact on the PL properties of ZnO:Er^{3+} nanocrystals was systematically studied for the first time. We have synthesized ZnO:Er^{3+} nanocrystals with controllable morphologies by the cetyltrimethylammonium bromide (CTAB)-assisted hydrothermal process. PL of the as-prepared ZnO was found to be significantly dependent on the morphology as well as crystallinity. Especially, with excitation at 980 nm, morphology influence on the Er^{3+}-related upconversion luminescence was studied.

2. Experimental section

All the chemicals were analytic grade reagents without further purification. $Zn(OH)_4^{2-}$ precursor solution was prepared by mixing 0.5 mol/L aqueous solution of $Zn(OAc)_2$ and $Er(OAc)_3$ with a molar ratio Zn/Er~98:2

**Also to be corresponded to.
*Corresponding author. Tel.: +31 20 525 6976; fax: +31 20 5255604.
E-mail addresses: xgkong14@ciomp.ac.cn (X. Kong), h.zhang@uva.nl (H. Zhang).

0022-2313/$ - see front matter © 2007 Elsevier B.V. All rights reserved.
doi:10.1016/j.jlumin.2007.04.011

Table 1
Summarized morphologies and reaction conditions

Number	Morphology	Reaction condition	Alkali metal hydroxide	Temperature (°C)	Reaction time (day)
1	Nanorod	10 mL of $[Zn(OH)_4]^{2-}$ solution/10 mL of 10% CTAB solution	NaOH	150	4
2	Prickly sphere-like	8 mL of $[Zn(OH)_4]^{2-}$ solution/2 g of CTAB	NaOH	180	2
3	Column-like	10 mL of $[Zn(OH)_4]^{2-}$ solution/10 mL of 10% CTAB solution/5 mL of methanol	NaOH	160	3
4	Branch rod-like	10 mL of $[Zn(OH)_4]^{2-}$ solution/10 mL of 10% CTAB solution/5 mL of ethanol	NaOH	180	3
5	Prism-like	15 mL of $[Zn(OH)_4]^{2-}$ solution/1 g of CTAB	LiOH	180	2
6	Grain-like	10 mL of $[Zn(OH)_4]^{2-}$ solution/10 mL of 10% CTAB solution/5 mL of methanol	LiOH	160	3

and 5 mol/L alkali solutions (volume ratio, v/v = 1:1, pH~14). ZnO:Er^{3+} nanostructure was prepared as follows. $Zn(OH)_4^{2-}$ precursor solution and 10% CTAB solution were mixed at a volume ratio of 1:1 in a vessel under constant stirring, resulting in a white aqueous solution which was then transferred into a 60 mL Teflon-lined stainless-steel autoclaves, sealed, and maintained at a given temperature for certain time before being slowly cooled to room temperature. The white precipitate deposited in the bottom of the autoclave was collected and washed several times with absolute ethanol and distilled water. The ZnO:Er^{3+} samples were obtained by centrifugation and dehydration of the precipitate in a vacuum at 50–60 °C. The reaction parameters for each series are summarized in Table 1. In this study, all samples were prepared with 2.0 mol% of Er. The morphology of ZnO:Er^{3+} is subject to reaction conditions, such as temperature, time, reactant concentration and react media. Varying these factors leads to the morphology of nanorod, column-like, prickly sphere-like, branch rod, prism-like or grain-like.

The sizes and morphologies of ZnO:Er^{3+} samples were characterized by scanning electron microscopy (SEM, JEOL, JSM-6700F), field emission SEM (FESEM, Hitachi, S-4800) and transmission electron microscopy (TEM, Hitachi, H-8100IV) operating at 200 kV accelerating voltage. High-resolution TEM (HRTEM) was realized by using a JEOL 2010 microscope operating at 200 kV. A small drop of the sample redispersed by ethanol was deposited on silicon substrate for SEM observation and on a copper grid that was pre-coated with a film of carbon then dried in the air for TEM characterization. Dry powder samples were used for the XRD (Rigaku, D/max rA, Cu Kα radiation) structural measurements. The room-temperature photoluminescence spectra were measured using a Jobin Yvon-LabRam Raman spectrometer and a Peltier air-cooled CCD detector. Samples were excited either by 325 nm line of a He–Cd laser or utilizing a semiconductor CW diode laser at 980 nm in case of up-conversion PL experiment. In the measurement of the excitation power dependence excitation beam was focused on the sample in an area of ~0.2 mm in diameter. In the luminescence decay measurements, the excitation was realized by 488 nm laser line of 2.7 ns pulse width at 10 Hz repetition rate (coherent infinity).

3. Results and discussion

Fig. 1 shows the XRD patterns of the ZnO:Er^{3+} powders. For all the samples (numbered from 1 to 6), the diffraction peaks are well assigned to hexagonal phase ZnO reported in JCPDS card (no. 36-1451). The very weak shoulders can be ascribed to hexagonal $Er(OH)_3$. The morphologies and reaction conditions are summarized in Table 1 and the representative SEM and TEM images are shown in Figs. 2 and 3. The lattice fringes of the HRTEM image (Fig. 2b) recorded from the edge of an individual nanorod are perpendicular to the long axis of ZnO and the well-resolved interference fringe spacing is about 0.364 nm, which is consistent with the *c*-axis parameter in the hexagonal ZnO phase. The average diameters of the ZnO:Er^{3+} perpendicular to the *c*-axis were evaluated from the XRD patterns by Scherrer formula employed on (0 0 2) diffraction peaks, as well as from the TEM and FESEM measurements, and both results were comparable (see Table 2).

There were reports on the growth kinetics and crystallization of ZnO in aqueous solution and alcohol–water medium [12,13]. The effect of the used alkali metal hydroxide molecules on the formation behavior of the zinc oxide was also examined [14]. In our experiments, temperature, reaction time and capping molecules were the key parameters. In solution containing the surfactant and inorganic reagent, CTA^+–$[Zn(OH)_4]^{2-}$ ion pairs were formed initially by electrostatic interaction between the CTAB surfactant and the $[Zn(OH)_4]^{2-}$, followed by a complexing agent formed via the assembly of CTA^+–$[Zn(OH)_4]^{2-}$ ion pairs under hydrothermal condition. The complexing agent was adsorbed on the circumference of the ZnO nuclei, which decreased the surface energy of ZnO nuclei, and resulted in active sites on the

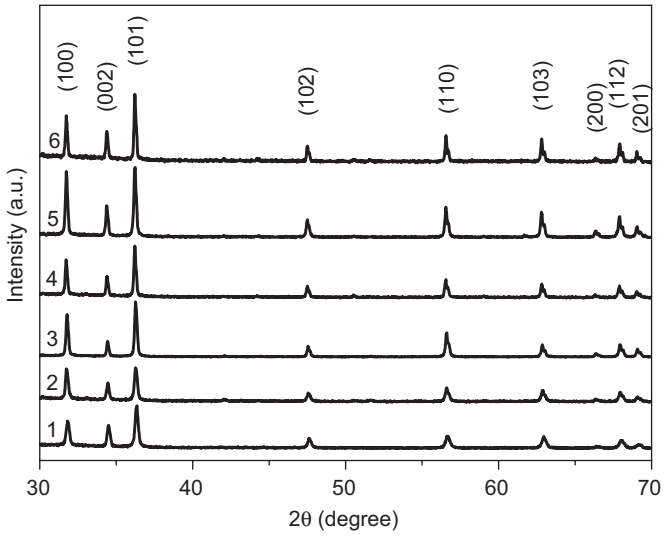

Fig. 1. XRD patterns of ZnO:Er^{3+} samples 1–6.

surface, and thus facilitated the growth of ZnO crystals on those active sites with different morphologies.

Room-temperature PL spectra of ZnO:Er^{3+} of various morphologies are shown in Fig. 4. It is obvious that the PL spectrum of ZnO depends on morphology under direct excitation, more specific 325 nm. Most samples evidence two emission bands: a narrow UV band around 390 nm and a broad visible band locating in the range of 450–640 nm, of which the former one is well known to come from the exciton recombination, whereas the latter is usually ascribed to the defects that affect the position as well as the shape of the band-edge emission [15]. Since the defect density is higher on the surface than in the bulk [16], various spectral shapes are expected in nanostructures of different sizes and morphologies which result in different surface-to-volume ratios. van Dijken et al. [17] have proposed that the particle surface plays a role in the process leading to the visible emission. The relative intensities of the UV and visible emissions in Fig. 4 are

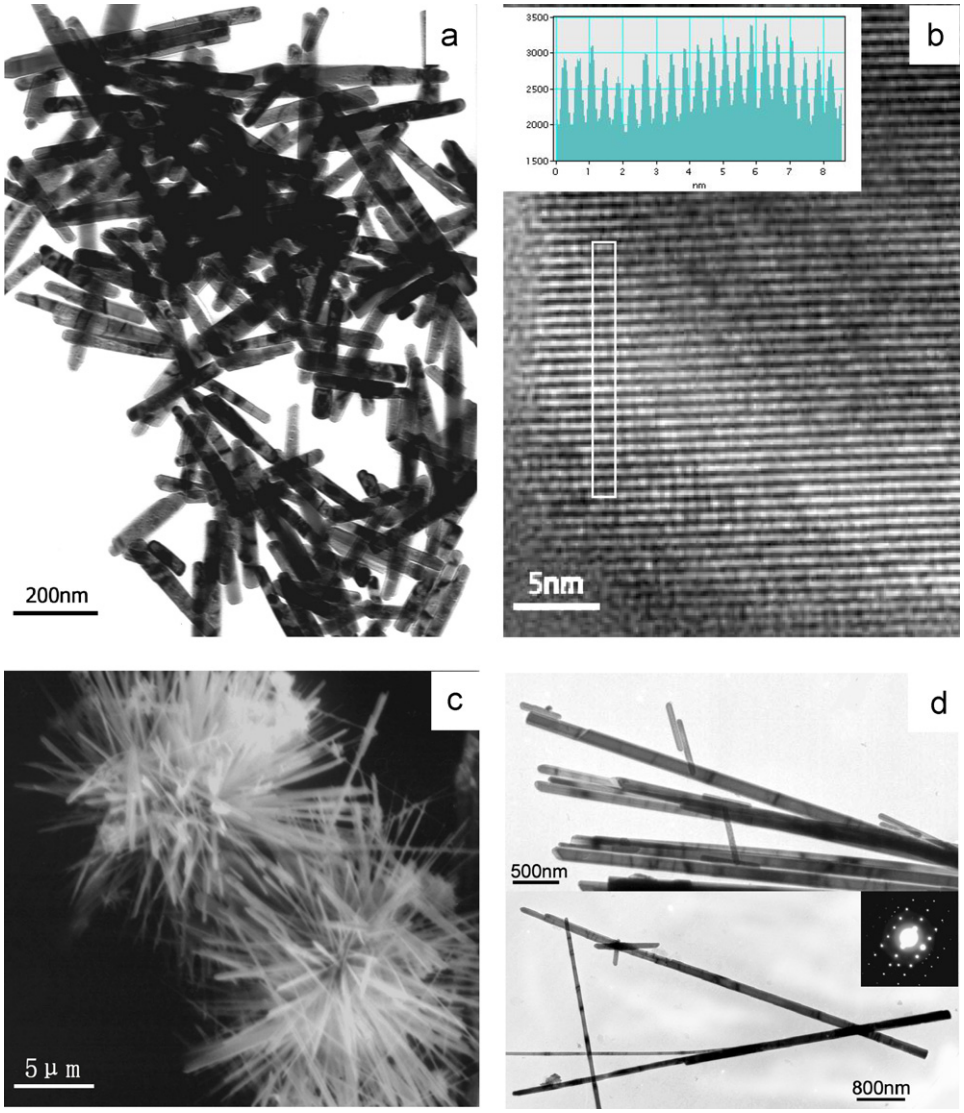

Fig. 2. TEM (a), HRTEM (b) images of samples 1 and SEM (c), TEM (d) of sample 2.

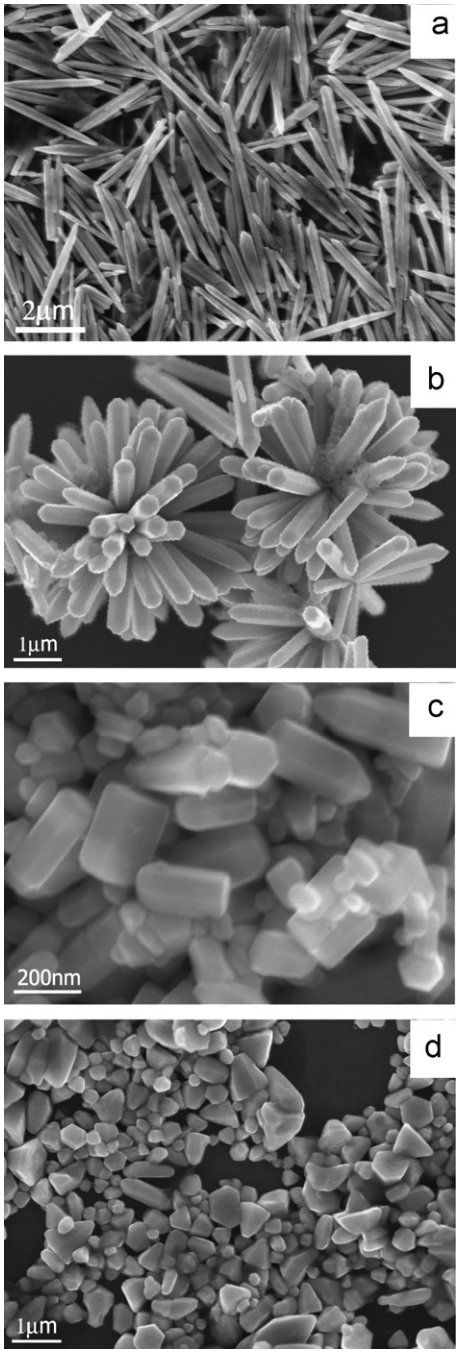

Fig. 3. FESEM images of sample 3–6: (a) column-like, (b) branch rod, (c) prism-like and (d) grain-like.

Table 2
The average diameter perpendicular to *c*-axis of the ZnO:Er^{3+} samples 1–6

Number	Morphology	2θ (°)	Size (nm)	
			XRD (002)	TEM and FETEM
1	Nanorod	34.50	68.6	60
2	Prickly sphere-like	34.46	102.9	109
3	Column-like	34.44	205.7	217
4	Branch rod-like	34.46	205.7	238
5	Prism-like	34.38	137.1	118
6	Grain-like	34.38	205.7	231

In XRD measurements, Scherrer formula is employed in the calculation. The size assessment from TEM and FESEM images is by averaging 100 particles for each sample.

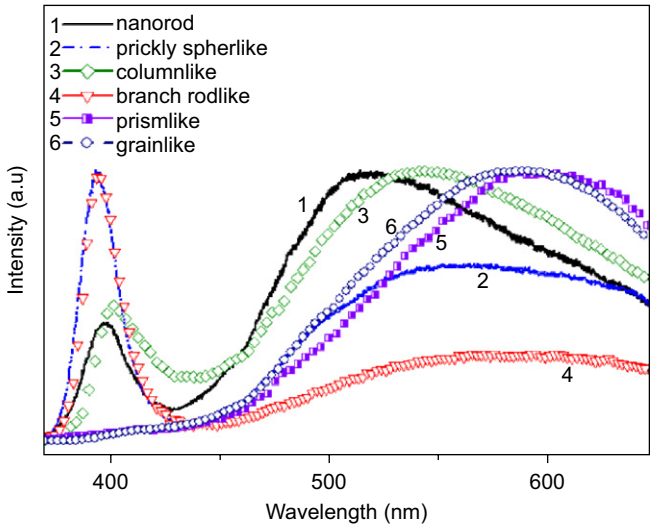

Fig. 4. Room-temperature PL spectra of ZnO:Er^{3+} samples 1–6 of various morphologies under 325 nm excitation.

obviously subject to the nanocrystal morphology, and the ratio of the two emissions can be taken as a measure of the crystalline quality [15]. As is shown in Fig. 4, the visible emission is stronger than UV emission for the nanorod and the column-like samples, whereas the UV emission is stronger than the visible emission for the prickly sphere- and the branch rod-like samples. In addition, the UV emission is not distinct for the prism- and the grain-like samples. Based on these results, it can be concluded that the prickly sphere- and the branch rod-like samples are superior, and the prism- and the grain-like samples are inferior in crystalline quality.

Furthermore, we would like to discuss the defect emission. The green emission-related surface defects are often assigned to singly ionized oxygen vacancy [18–20], although this assignment is highly controversial. Interstitial oxygen and Li impurities were proposed in the literatures to be the defects in the bulk responsible for the yellow emission [21–23]. Moreover, the volume defect content strongly depends on the crystal preparation process [24]. From this point of view, it can be argued that the prism- and grain-like samples have more internal defect contents than other samples, leading to the yellow emission and worse crystalline quality, due to the use of the LiOH as alkali in the synthetic process.

Upconversion luminescence of Er^{3+} is attractive because it, to a large extent, is background free compared with direct excitation. In order to perform the study on the morphology influence on the upconversion luminescence,

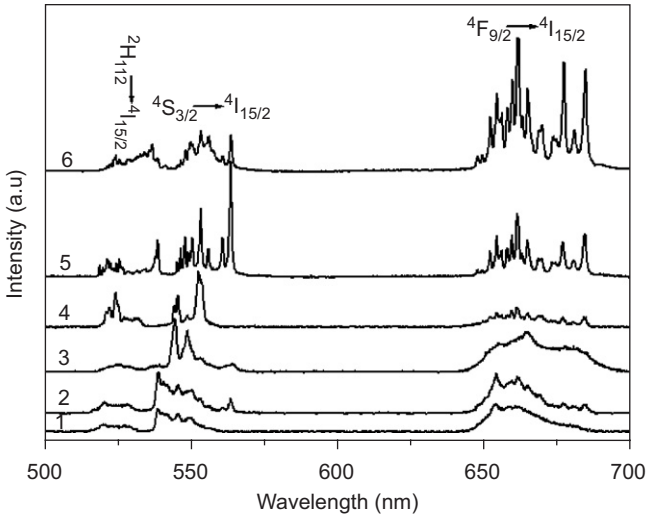

Fig. 5. Room-temperature visible upconversion emission spectra of ZnO:Er^{3+} with various morphologies upon excitation at 980 nm.

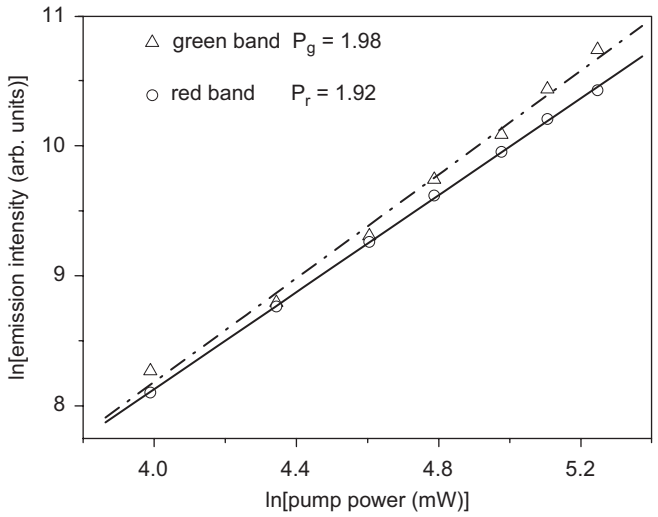

Fig. 6. Excitation power dependence of the upconverted green ($^2H_{11/2}$ ($^4S_{3/2}$)$\rightarrow{}^4I_{15/2}$) and red ($^4F_{9/2}\rightarrow{}^4I_{15/2}$) emissions of the grain-like sample. The best fitting results with the function described in the text are given in solid and dash-dotted lines.

all ZnO:Er^{3+} samples were annealed at 700 °C for 30 min in air. Upon continuous 980 nm infrared irradiation, the up-converted emission of Er^{3+} was observed in visible region as is shown in Fig. 5. The upconversion mechanism of erbium ion in the different matrix has been extensively discussed by, e.g. Güdel and co-worker [25] and Auzel [26]. The upconversion emission mechanism comprises several processes, including excited-state absorption (ESA) and energy transfer (ET) between excited neighboring Er^{3+} ions [26]. Ensuing sequential two-photon absorption of Er^{3+} ($^4I_{15/2}\rightarrow{}^4I_{11/2}$, $^4I_{11/2}\rightarrow{}^4F_{7/2}$), the populated $^4F_{7/2}$ level nonradiatively relaxes to $^2H_{11/2}$ and $^4S_{3/2}$ levels, producing the green emission. The $^4S_{3/2}$ level can also decay nonradiatively to $^4F_{9/2}$ level, producing partly the red emission. The relaxation from the populated $^4I_{11/2}$ state to the $^4I_{13/2}$ state offers another channel of feeding the $^4F_{9/2}$ state, via a phonon-assisted excitation. From the excitation power dependence of the upconversion luminescence the mechanism can be distinguished to a great extent. The excitation power dependence was determined for both the green ($^2H_{11/2}$,$^4S_{3/2}$)$\rightarrow{}^4I_{15/2}$) and the red ($^4F_{9/2}\rightarrow{}^4I_{15/2}$) emissions. Typical example is shown in Fig. 6. In general, such a dependence can be formulated as [26]

$$I \propto I_{\mathrm{exc}}^{P},$$

where I is the upconverted emission intensity, I_{exc} is the excitation laser power and P is related with the number of the pump photons absorbed per emit photon. Fitting the data with this function results in P equals to 1.98 and 1.92 for the green and the red emissions, respectively. The values are very close to 2—an unambiguous evidence that the upconversion process in our samples is dominated by the ESA mechanism.

It is clear from Fig. 5 that not only the ratio of the green and the red emissions, but also the relative intensities of the emissions from various Stark levels of Er^{3+} are different in various ZnO nanostructures. For samples 1 and 2, the emissions have broad transition lines and the intensities of the green and the red bands are comparable, whereas sharp lines appear for samples 5 and 6 and the red emission is stronger than the green one for sample 6. These differences underline the variation of the Er^{3+} local structure [27]. It was reported that the optically active Er^{3+} center in ZnO is an ErO_6 complex, where Er is located at the center of an oxygen octahedron with unequal edge lengths. In our experiments, however, this scenario is only one of the possibilities. Other factors, like defects around Er^{3+} etc. cannot be ruled out. In fact, solubility of Er^{3+} in ZnO is low [28,29] because the radius of Er^{3+} ion (0.88 Å) is larger than that of the Zn^{2+} ion (0.74 Å), and their formal valences are different. On the other hand, recent hypothesis about doping in semiconductor proposed also that the doping efficiency is determined by surface morphology, nanocrystal shape, and surfactant in the growth solution based on kinetics [30]. Both mechanisms lead to the same conclusion consistent with the experimental fact that introducing Er^{3+} ions into the ZnO host in nanosize is not an easy task. Usually only a minor fraction of the total amount of the Er^{3+} goes into the Zn substitutional positions, and most Er^{3+} ions reside on the surface or on the grain boundaries of the ZnO crystals to yield optimum strain relief. Thus, the distribution of the doped erbium ions in ZnO matrix was not the same for all ZnO samples because their morphologies are different.

The excitation power dependence of the upconversion luminescence is in line with this conclusion. As mentioned above, the power dependence illustrates that the dominant upconversion mechanism is ESA and ET mechanism can be ignored (P is very close to 2). Note that the nominal doping concentration was pretty high, i.e. Zn/Er ratio was 98:2. If the real doping concentration were similarly high the energy transfer between Er^{3+} ions could not be ignored

in upconversion process. Therefore, the real doping concentration must be much lower.

At this end, it is important to discuss the influence of the possibly formed Er_2O_3 nanocrystals. During the synthetic process, the presence of some Er_2O_3 nanocrystals was inevitable, which might also contribute to the observed upconversion luminescence. To validate our assignment that the observed emission is primarily originated from ZnO:Er^{3+}, we have compared the spectral characteristics of Er^{3+} doped in ZnO and in Er_2O_3 nanocrystals. Er_2O_3 nanocrystals of size between 5 and 30 nm were reported to show broad visible upconversion luminescence bands with lifetime around 93 μs when detected at 543 nm [31], and to remain the broad feature when immersed in Titania/organically modified silane composites [32]. This is different from the distinct structure observed in the visible upconversion spectra of our samples. In addition, for the Er_2O_3 nanocrystals, the upconversion excitation peak is shifted to 993 nm, whereas 980 nm—a wavelength for upconversion excitation of our ZnO:Er^{3+} samples—cannot efficiently excite the Er_2O_3 nanocrystals. Based on these arguments, it is rational to believe that the observed upconversion luminescence is mainly due to ZnO:Er^{3+} nanocrystals. However, at the moment, we cannot provide a quantitative assessment on the existence of the Er_2O_3.

Luminescence decay traces have been recorded for various ZnO:Er^{3+} samples, the typical ones are summarized in Table 3. As can be seen from the table, every decay curve can be well fitted by a bi-exponential function. For the green emission (~545 nm), the shorter one is lengthened from several hundred nanoseconds for samples 1, 2, 4 to several microseconds for samples 5, 6, whereas the longer component in the mean time changes from several microseconds to ~30 μs. The luminescence quantum yield of ZnO:Er is, in general, less than 5% for the green and the red emissions. These values are short compared to that of the Er^{3+} doped in similar bulk materials [33,34]. The lengthening of the decay and the increase of the estimated quantum yield in samples 5 and 6, compared with the rest samples, reveal that the luminescence quenching is less for the two, probably indicating that in these two samples more Er^{3+} ions were doped into the internal area of ZnO, different from the rest samples where majority of Er^{3+} ions were within the surface layer, if not all of them.

Moreover, the organic surfactant molecules (CTAB) were coupled to the surface of ZnO in the synthetic process, which hampered the emission structure of Er^{3+}. The nanorod (sample 1) and column-like (sample 3) samples own similar rod-like shape, but sample 3 has faced structure and lager size. Similarly, the shapes of samples 2 and 4 are close to flower-like, whereas the sample 4 has good hexagonal faces and smaller surface-to-volume ratio. Eilers and Tissue [36] reported the effect of particle size on the spectra, where the emission lines are getting broadened when the particle size decreases. Besides, it is confirmed that certain crystalline faces facilitate doping [30]. Thus, more Er^{3+} ions are expected to come into samples 3 and 4 than samples 1 and 2. The relatively high doping efficiency results in the sharp transition lines for samples 3 and 4, similar to the case of bulk materials. Whereas the emission line broadening of samples 1 and 2 can be ascribed to the surface effect due to the relatively large surface-to-volume ratio. As far as the prism- (5) and grain-like (6) samples are concerned, sharp emissions are also present, which indicates more contribution of the interior Er^{3+} ions. As mentioned above, for samples 5 and 6 alkali LiOH was added in the synthetic process, differing from the rest samples where NaOH was used. As the radius of the Li^+ ion (0.76 Å) is small comparing with Na^+ ion (1.02 Å) and close to that of Zn^{2+} ion (0.74 Å), the Li^+ ions can occupy the substitutional Zn^{2+} sites and interstitial sites in ZnO crystalline lattice and in/near ErO_6 to maintain a local charge balance between the Er^{3+} and the Li^+ in the ZnO lattice. Furthermore, large space between Er and O in ErO_6 structure may accelerate the trend of Li^+ occupying in/near ErO_6. Therefore, adding LiOH facilitated the doping of Er^{3+} into the ZnO lattice, resulting in more extinct fine structure in Er^{3+} emission.

At last, we want to comment on the relative intensity issue. As mentioned above, the intensity ratio of the green to the red emissions shows morphology dependence. It is well established that the upconversion efficiency is mainly

Table 3
Bi-exponential fitting results of luminescence decay transients for the ZnO:Er^{3+} of various morphologies (after annealing at 700 °C) under 488 nm pulsed excitation

Morphology	$(^2H_{11/2}, {}^4S_{3/2}) \rightarrow {}^4I_{15/2}$				$^4F_{9/2} \rightarrow {}^4I_{15/2}$			
	τ_1 (μs)	τ_2 (μs)	Mean lifetime (μs)	Quantum yield[a] (%)	τ_1(μs)	τ_2 (μs)	Mean lifetime (μs)	Quantum yield[a] (%)
Nanorod	0.34 (88%)	3.06 (12%)	0.666	0.36	0.27 (92%)	3.28 (8%)	0.446	0.24
Prickly sphere-like	0.32 (89%)	3.75 (11%)	0.697	0.37	0.34 (91%)	4.99 (9%)	0.759	0.41
Branch rod-like	0.55 (73%)	2.51 (27%)	1.08	0.58	0.43 (86%)	5.28 (14%)	1.11	0.60
Prism-like	0.59 (85%)	28.4 (15%)	4.76	2.6	0.26 (33%)	3.29 (67%)	2.29	1.2
Grain-like	1.47 (79%)	28.8 (21%)	7.21	3.8	0.35 (55%)	2.24 (45%)	1.20	0.65

[a]The quantum yield is calculated as $\tau_{fl}/(\tau_{fl}+\tau_r)$, where τ_{fl} is taken from the measurements and τ_r is from Ref. [34].

determined by the nonradiative processes of the host lattice [37], and the red emission ($^4F_{9/2} \rightarrow {}^4I_{15/2}$) can be produced via (1) nonradiative relaxation through the $^4S_{3/2}$ excited state and (2) relaxation from the $^4I_{11/2}$ state to the $^4I_{13/2}$ state, followed by a phonon-assisted excitation into the $^4F_{9/2}$ state. In general, the energy gap of $\sim 3000\,cm^{-1}$ between the $^4S_{3/2}$ and $^4F_{9/2}$ levels is not efficiently bridged by multiphonon processes because of the low phonon energy ($\sim 400\,cm^{-1}$) of the ZnO host. However, the multiphonon relaxation becomes effective in these nanocrystals due to the presence of some organic groups of high-energy vibrational quanta on the surface of the crystals, e.g. O–H, C=O, etc. Those groups exist even after high-temperature annealing [38]. The density of the organic groups on the surface is subject to morphology because surface-to-volume ratio is morphology dependent; consequently, the relative intensity between the green and the red emissions is also morphology dependent. On the other hand, higher distribution of active ions in the matrix benefits to the red emission owing to the fact that short distance between the Er^{3+} ions which assists the energy transfer process [39]. In our experiment, since sample 6 has small surface-to-volume ratio, relative to sample 5, the internal concentration of Er^{3+} is relatively higher, thus the red emission is enhanced for sample 6.

In conclusion, the emission of hydrothermally prepared Zn:Er^{3+} nanocrystals has been systematically studied as a function of morphology. The exciton and defect emissions under UV excitation and the upconversion Er^{3+} emission detectable only under IR excitation, demonstrate the significant influence of the morphology, which was concluded to be the consequence of the morphology effect on the local environments around Er^{3+} ions and doping efficiency, as well as the density and distribution of the organic groups on the surface.

Acknowledgment

This work was supported by NSFC of China (60601014 and 20603035), exchange program between CAS of China and KNAW of the Netherlands and the Major Foundation of Chinese Academy of Sciences (kjcx2-sw-h12-02). The authors are grateful to Prof. S.H. Huang from Beijing Jiaotong University of China for simulating discussion on the excited state dynamics of rare-earth ions. H.J. Ramesdonk (UvA) is gratefully acknowledged for his technical assistance in luminescence decay measurements.

References

[1] M.H. Huang, S. Mao, H. Feick, H.Q. Yan, Y.Y. Wu, H. Kind, R. Russo, P.D. Yang, Science 292 (2001) 1897.
[2] H. Kind, H. Yan, B. Messer, M. Law, P. Yang, Adv. Mater. 14 (2002) 158.
[3] P. Yang, H. Yan, S. Mao, R. Russo, J. Johnson, R. Saykally, N. Morris, J. Pham, R. He, H.-J. Choi, Adv. Funct. Mater. 12 (2002) 323.
[4] G. Blasse, B.C. Grabmaier, Luminescent Materials, Springer, Berlin, 1994.
[5] A.K. Pradhan, K. Zhang, G.B. Loutts, U.N. Roy, Y. Cui, A. Burger, J. Phys.: Condens. Matter 16 (2004) 7123.
[6] S. Coffa, G. Franzo, F. Priolo, A. Polman, R. Serna, Phys. Rev. B 49 (1994) 16313.
[7] J.H. Shin, G.N. Van den Hoven, A. Polman, Appl. Phys. Lett. 67 (1995) 377.
[8] J.W. Stouwdam, F.C.J.M. van Veggel, Chem. Phys. Chem. 5 (2004) 743.
[9] A. Taguchi, K. Takahei, J. Appl. Phys. 83 (1998) 2800.
[10] G.G. Zegrya, V.F. Masterov, Appl. Phys. Lett. 73 (1998) 3444.
[11] S. Komuro, T. Katsumata, T. Morikawa, X. Zhao, H. Isshiki, Y. Aoyagi, Appl. Phys. Lett. 74 (1999) 377.
[12] C. Pacholski, A. Kornowski, H. Weller, Angew. Chem. Int. Ed. 41 (2002) 1188.
[13] E.M. Wong, J.E. Bonevich, P.C.J. Searson, Phys. Chem. B 102 (1998) 7770.
[14] N. Uekawa, R. Yamashita, Y.J. Wu, K. Kakegawa, Phys. Chem. Chem. Phys. 6 (2004) 442.
[15] A.B. Djurišić, Y.H. Leung, Small 2 (2006) 944.
[16] W. Göpel, U. Lampe, Phys. Rev. B 22 (1980) 6447.
[17] A. van Dijken, E.A. Meulenkamp, D. Vanmaekelbergh, A. Meijerink, J. Phys. Chem. B 104 (2000) 1715.
[18] H.T. Ng, B. Chen, J. Li, J. Han, M. Meyyappan, J. Wu, S.X. Li, E.E. Haller, Appl. Phys. Lett. 82 (2003) 2023.
[19] Z. Chen, N. Wu, Z. Shan, M. Zhao, S. Li, C.B. Jiang, M.K. Chyu, S.X. Mao, Scripta Mater. 52 (2005) 63.
[20] X. Liu, X. Wu, H. Cao, R.P.H. Chang, J. Appl. Phys. 95 (2004) 3141.
[21] L.E. Greene, M. Law, J. Goldberger, F. Kim, J.C. Johnson, Y. Zhang, R.J. Saykally, P. Yang, Angew. Chem. Int. Ed. 42 (2003) 3031.
[22] Y.W. Heo, D.P. Norton, S.J. Pearton, J. Appl. Phys. 98 (2005) 073502.
[23] D. Li, Y.H. Leung, A.B. Djurišić, Z.T. Liu, M.H. Xie, S.L. Shi, S.J. Xu, W.K. Chan, Appl. Phys. Lett. 85 (2004) 1601.
[24] D. Millers, L. Grigorjeva, W. Lojkowski, T. Strachowski, Rad. Meas. 38 (2004) 589.
[25] P. Gerner, H.U. Güdel, Chem. Phys. Lett. 413 (2005) 105.
[26] F. Auzel, Chem. Rev. 104 (2004) 139.
[27] M. Ishii, S. Komuro, T. Morikawa, Y. Aoyagi, J. Appl. Phys. 89 (2001) 3679.
[28] W.M. Jadwisienczak, H.J. Lozykowski, A. Xu, B. Patel, J. Electron. Mater. 31 (2002) 776.
[29] S. Bachir, K. Azuma, J. Kossanyi, P. Valat, J.C. Ronfard-Haret, J. Lumin. 75 (1997) 35.
[30] S.C. Erwin, L. Zu, M.I. Haftel, A.L. Efros, T.A. Kennedy, D.J. Norris, Nature 436 (2005) 91.
[31] W.X. Que, S. Buddhudu, Y. Zhou, Y.L. Lam, J. Zhou, Y.C. Chan, C.H. Kam, L.H. Gan, G.R. Deen, Mater. Sci. Eng. C 16 (2001) 51.
[32] W.X. Que, Y. Zhou, Y.L. Lam, K. Pita, Y.C. Chan, C.H. Kam, Appl. Phys. A 73 (2001) 209.
[33] F. Vetrone, J.-C. Boyer, J.A. Capobianco, A. Speghini, M. Bettinelli, Appl. Phys. Lett. 80 (2002) 1752.
[34] R. Rolli, K. Gatterer, M. Wachtler, M. Bettinelli, A. Speghini, D. Ajò, Spectrochim. Acta Part A 57 (2001) 2009.
[36] H. Eilers, B.M. Tissue, Chem. Phys. Lett. 251 (1996) 74.
[37] F. Vetrone, J. Christopher Boyer, J.A. Capobianco, J. Phys. Chem. B 106 (2002) 5622.
[38] J.A. Capobianco, F. Vetrone, J.C. Boyer, A. Speghini, M. Bettinelli, J. Phys. Chem. B 106 (2002) 1181.
[39] S. Xiao, X. Yanga, Z. Liu, X.H. Yan, Opt. Mater. 28 (2006) 285.